Supplementary Information (SI) for Materials Horizons.

Supplementary Information

Efficient solar-driven freshwater generation through an inner hierarchical porous metal-carbon layer bridging synergistic photothermal evaporation and adsorption-photodegradation

Haoyu Liu [a], Huaipeng Pang [a], Xinyu Yang [a], Wenhao Guo [a], Hongyan Xi [a], Xueli Ji [a], Lin Li [b], Fanlu Meng [a,*]

[a] School of Materials Science and Engineering, Ocean University of China, Qingdao 266404, China.

[b] Electron Microscopy Center, Jilin University, Changchun, 130012 China.

E-mail: mengfanlu@ouc.edu.cn.

Materials: Balsa wood was purchased from Shengyuan Wood Industry Co., Ltd. Cobalt nitrate hexahydrate ($Co(NO_3)_2 \cdot 6H_2O$, 99%) and 2-methylimidazole (2-MeIm, 98%) were purchased from Macklin Reagents Ltd. (Shanghai, China). Bismuth nitrate pentahydrate ($Bi(NO_3)_3 \cdot 5H_2O$, 99%), potassium bromide (KBr, 99%), triethanolamine (TEOA, AR) and rhodamine B (RhB, AR) were purchased from Aladdin Reagents Ltd. (Shanghai, China). Ethylene glycol ($(CH_2OH)_2$, AR), isopropyl alcohol (IPA, AR) and ethanol (C_2H_5OH, AR) were purchased from Sinopharm Chemical Reagent Co., Ltd. (Shanghai, China). P-benzoquinone (BQ, > 98.0%) was purchased from TCI Development Co., Ltd. (Shanghai, China). All water used in the experiment was deionized water.

Synthesis of ZIF-67@Wood (ZW), carbonized ZIF-67@Wood (ZCW), and carbonized Wood (CW): Balsa wood blocks ($15 \times 15 \times 15$ mm^3) were prepared, cutting across the grain. A solution of 40 mmol $Co(NO_3)_2 \cdot 6H_2O$ in 80 mL of a 1:1 mixture of absolute ethanol and deionized water was made. These blocks were then soaked in this solution, undergoing two cycles of 30 minutes each under vacuum and then atmospheric pressure. Following this, the soaked blocks were autoclaved in a 100 mL Teflon-lined stainless-steel vessel at 80°C for 14 hours. Afterward, a similar procedure was followed using 40 mmol of 2-MeIm in the same ethanol-water mixture for impregnation and hydrothermal treatment. Post-reaction, the samples were rinsed with deionized water to clean surface particles and then freeze-dried under vacuum for 48 hours using a vacuum freeze dryer to yield the final ZW product. The ZW were pyrolysis in a three-step process in a tube furnace. First, carbonized at 200°C for 2 hours (3°C min^{-1}), then at 500°C for 1 hour (5°C min^{-1}), and finally, heated to 750°C for 2 hours (3°C min^{-1}) under a protective N_2 flow (100 mL min^{-1}). After cooling, the ZCW was produced. The synthesis of CW was conducted using the identical procedure as outlined for ZCW.

Synthesis of BiOBr@ZCW, BiOBr@CW, and BiOBr nanosheet: In a typical process, 0.5

mmol $Bi(NO_3)_3 \cdot 5H_2O$ was dissolved in 20 mL ethylene glycol, and 0.5 mmol KBr in 20 mL deionized water, each for 10 minutes, to prepare solutions A and B, respectively. After mixing both solutions and adding a piece of ZCW or CW, the mixture was transferred into a 50 mL Teflon-lined stainless-steel autoclave heated to 160°C for 8 hours. The final products, BiOBr@ZCW or BiOBr@CW, were washed, then dried at 60°C for 12 hours under vacuum. The BiOBr nanosheet was prepared without ZCW and CW using the same conditions. To assess the impact of BiOBr loading on the photodegradation performance, BiOBr@ZCW samples with different ratio between BiOBr and ZCW were prepared. For the synthesis of BiOBr@ZCW-0.5 and BiOBr@ZCW-1.5, the quantities of $Bi(NO_3)_3$ (with KBr in equimolar amounts) were adjusted to 0.5 mmol and 1.5 mmol, respectively.

Characterization:

The phase and crystal structure of the samples were examined by X-ray diffraction (XRD, Bruker D8) patterns using Rigaku X-ray diffractometer with Cu Kα radiation ($\lambda = 1.5406$ Å). The accelerating voltage and applied current were 40 kV and 40 mA, respectively. The morphology analysis of the samples was observed by scanning electron microscope (SEM, ZEISS Gemini 300) equipped with an EDX and the microstructure of the samples was characterized via a transmission electron microscope (TEM, JEOL JEM-2100F). The surface states of the samples were characterized by X-ray photoelectron spectroscopy (XPS, Thermo Fisher Scientific K-Alpha) with an Al Ka X-ray source (1486.6 eV). The binding energy was calibrated using the C1 s (284.8 eV). Raman spectrums were conducted on the samples using a Raman microscope (Lab RAM HR800). The functional groups and bonds of molecules were measured from 4000 cm^{-1} to 400 cm^{-1} using a fourier transform infrared spectrometer (FT-IR, Nicolet IS50). The pore structure of the samples was estimated using ASAP 2460 analyzer based on Nitrogen adsorption and desorption. Contact angles were measured using a contact angle meter (JC2000DM). UV-Vis-NIR reflectance spectra and UV-vis diffuse reflectance spectra (UV-vis DRS) were measured on a UV-Vis-NIR spectrometer (Daojin UV-3600 plus) equipped with an integrating sphere. The photoluminescence (PL, FluoroMax-4) spectra of the samples were meticulously studied at an excitation wavelength of 324 nm using a fluorescence spectrometer equipped with a slit width of 2 nm. The work function and valence band position of the material were determined through the application of UV photoelectron spectroscopy (UPS, ThermoFisher Escalab 250XI), which utilizes an energy spectrometer with a source gun of type He I. The presence of $\cdot O_2^-$ and $\cdot OH$ reactive radicals was identified via electron paramagnetic resonance (EPR, epr200 plus) spectroscopy, employing 5,5-dimethyl-1-pyrroline N-oxide (DMPO) as a trapping agent and a 300 W xenon lamp as a light source. The experimental conditions involved illuminating the sample under visible light for 1 min and in darkness, respectively. The concentration of metal ion was determined by inductively coupled plasma optical emission spectrometry (ICP, icpmsPE300D).

Photothermal water evaporation measurements:

The water evaporation tests were performed in a 100 mL small beaker at room temperature (~21°C) and the whole sample was placed in above beaker. During the water evaporation tests, small beaker was placed in a heat-proof square box (homemade using PS foam and PU sponge). For each run, small beaker was fully filled with water. 300 W xenon lamp (CEL-PF300-T8, Beijing China Education Au-light Co., Ltd.) equipped with a 420 nm filter was used to provide simulated sunlight. Radiation intensity (0.5, 1.0, 1.5, and 2.0 kW m^{-2}) was measured by optical power meter (LX-107, Shenzhen Vicimeter Technology Co., Ltd.). The mass change of the system was monitored by an electrical balance every 10 min. The average surface temperature was monitored by a FLIR i50 infrared camera (HM-TPH16-6VF/M, Hangzhou Microimage Software Co., Ltd.).

The energy efficiency (η) calculation of solar-steam conversion can be calculated using the following formula:

$$\eta = \frac{v\,\Delta h_{LV}}{P} \#(1)$$

Where v is the evaporation rate of water under solar illumination, P is the solar power density of 1 sun, and Δh_{LV} made up of the sensible heat and the enthalpy of vaporization is calculated using the following formula:

$$\Delta h_{LV} = C\,\Delta T + \ \Delta h \#(2)$$

Where C is the specific heat capacity of water and a constant of 4.18 J g^{-1} K^{-1}, ΔT is the temperature increase on the surface of the materials, and Δh is the relative enthalpy of vaporization of the water.

Photocatalytic degradation measurements:

The photocatalytic activities were evaluated through the degradation of RhB under light irradiation. Initially, a piece of BiOBr@ZCW (the weight is ~50 mg) was added into 100 mL of RhB solution (20 mg L^{-1}). Prior to irradiation, the suspension was slowly stirred in darkness for 30 min to guarantee an adsorption-desorption equilibrium. For comparison, identical experiments were conducted using either ZCW or 50 mg of BiOBr in lieu of BiOBr@ZCW. Subsequently, 6 mL suspension was collected at 5 min intervals. The supernatant was then analyzed using a UV-Vis spectrophotometer (UV-2600i) at an absorption wavelength of 554 nm to evaluate the RhB concentration. The degradation rate of RhB can be calculated by the following formula:

$$E_t = \left(1 - \frac{C_t}{C_0}\right) \times \ 100\% \#(3)$$

where C_0 and C_t are denoted as the initial concentration and the residual concentration of RhB at time t, respectively.

Meanwhile, the stability and recyclability of BiOBr@ZCW photocatalyst were investigated under the same operating conditions. In the cycle experiments, the samples used was collected, washed with deionized water, and then dried for 12 h at 60°C before the next test.

The photodegradation efficacy of BiOBr@ZCW was further evaluated by testing its performance on the degradation of other commonly used dyes, including methylene blue (MB), methyl orange (MO), and malachite green (MG). These experiments were conducted to assess the general applicability of BiOBr@ZCW across various dye systems.

The photoelectrochemical measurements were performed with a CHI760E electrochemical analyzer (CHI760E, Shanghai Chen Hua Instrument Co., China) in a three-electrode quartz cell setup, comprising the sample as the working electrode, a platinum foil counter electrode, and a saturated Ag/AgCl reference electrode, with 0.5 M Na_2SO_4 as the electrolyte. The working electrode was made up of a carbon paper with Nafion solution. Electrochemical impedance spectroscopy (EIS) measurement was carried out at open circuit potential with an ac perturbation of 5 mV. The Mott-Schottky curve was tested at the fixed frequencies of 500, 1000, and 1500 Hz.

Free radical trapping measurements:

The use of various organic inhibitors served to validate the active radicals involved in the photolysis process of Rhodamine B (RhB). Specifically, isopropanol (IPA, 1 mmol L^{-1}), p-benzoquinone (BQ, 1 mmol L^{-1}), and triethanolamine (TEOA, 1 mmol L^{-1}) were employed as scavengers for the hydroxyl radical (·OH), superoxide anion radical ($\cdot O_2^-$), and hole (h^+), respectively. In addition, we further conducted photodegradation experiments under a protective argon flow (Ar, 100 mL min^{-1}) to remove dissolved oxygen from the RhB aqueous solution, thereby eliminating the photogenerated $\cdot O_2^-$, in order to verify the degradation mechanism. The capture of these reactive radicals was performed during the photolysis of RhB (20 mg L^{-1}) under one sun illumination.

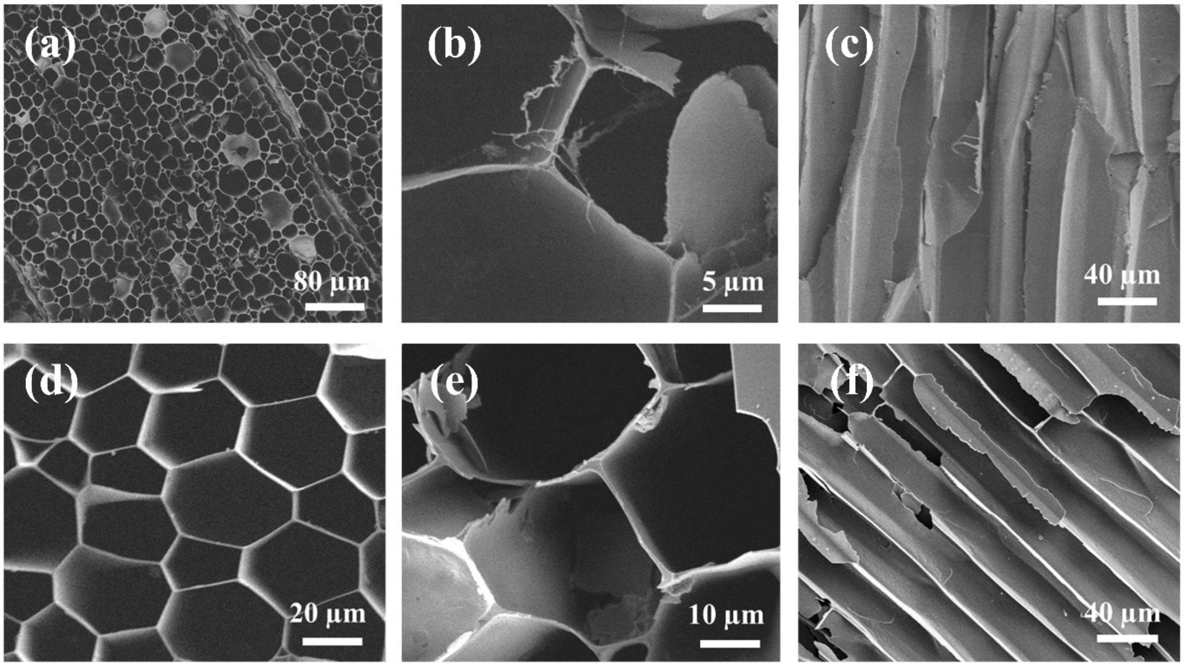

Fig. S1 SEM images of NW in the (a, b) vertical and (c) parallel direction. SEM images of CW in the (d, e) vertical and (f) parallel direction.

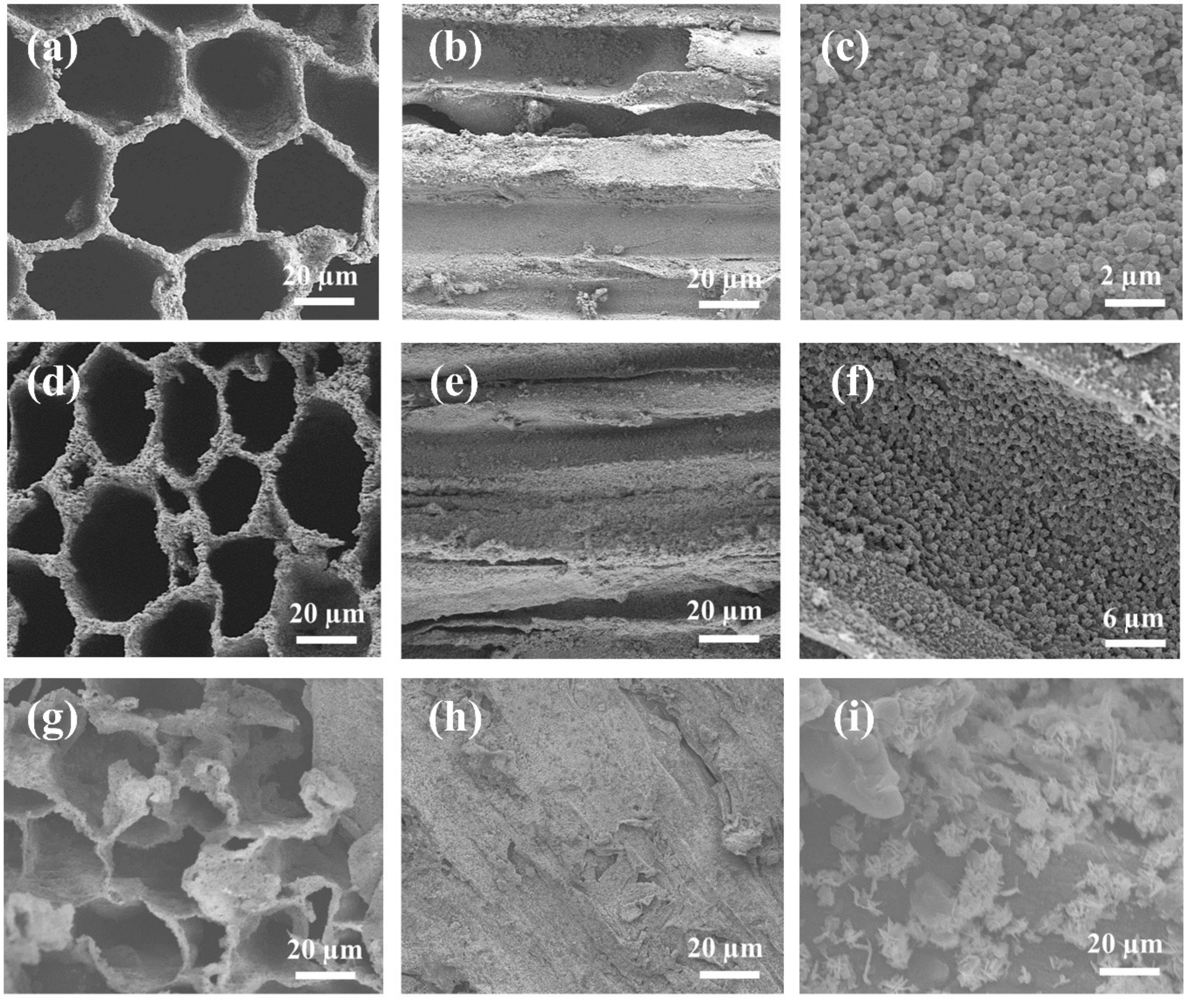

Fig. S2 SEM images of ZW in the (a) vertical and (b) parallel direction. (c) The microscopic morphology of ZW surface. SEM images of ZCW in the (d) vertical and (e) parallel direction. (f) The microscopic morphology of ZCW surface. SEM images of BiOBr@CW in the (g) vertical and (h) parallel direction. (i) The microscopic morphology of BiOBr@CW surface.

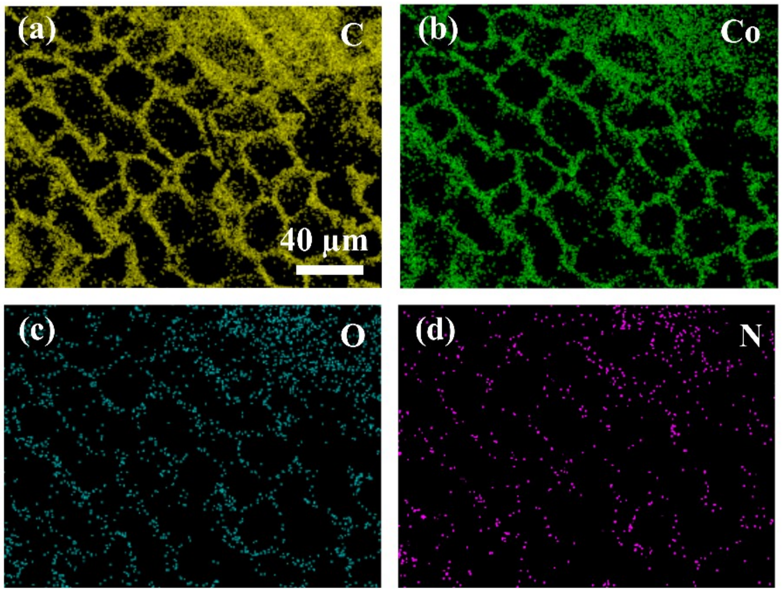

Fig. S3 EDS element mapping of (a) C, (b) Co, (c) O, and (d) N in ZCW in the parallel direction.

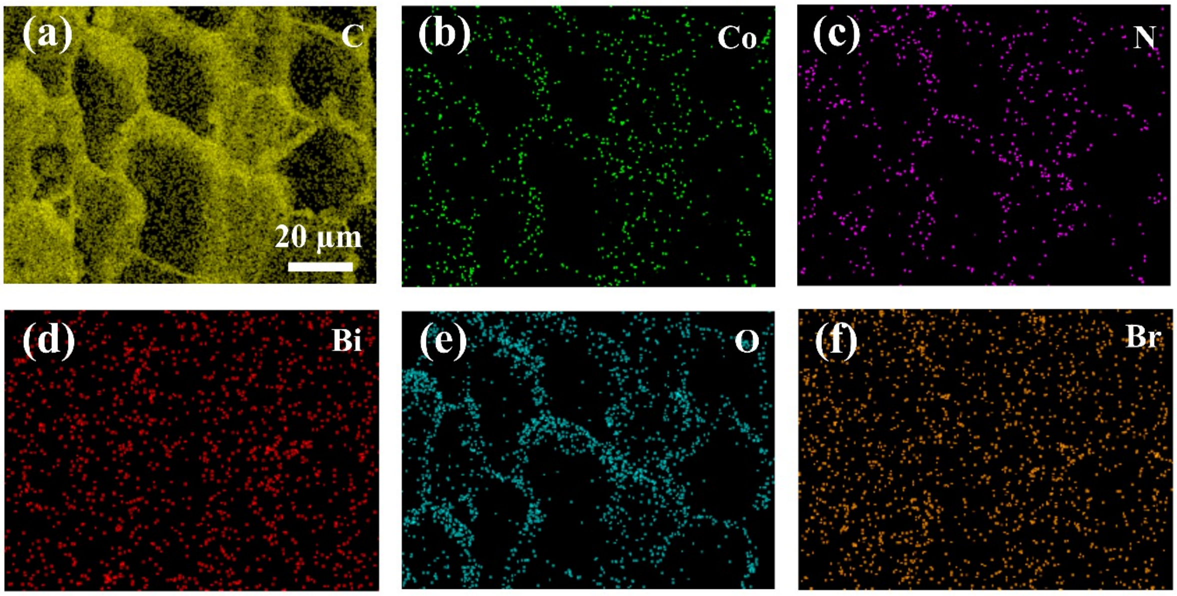

Fig. S4 EDS element mapping of (a) C, (b) Co, (c) N, (d) Bi, (e) O and (f) Br in BiOBr@ZCW in the parallel direction.

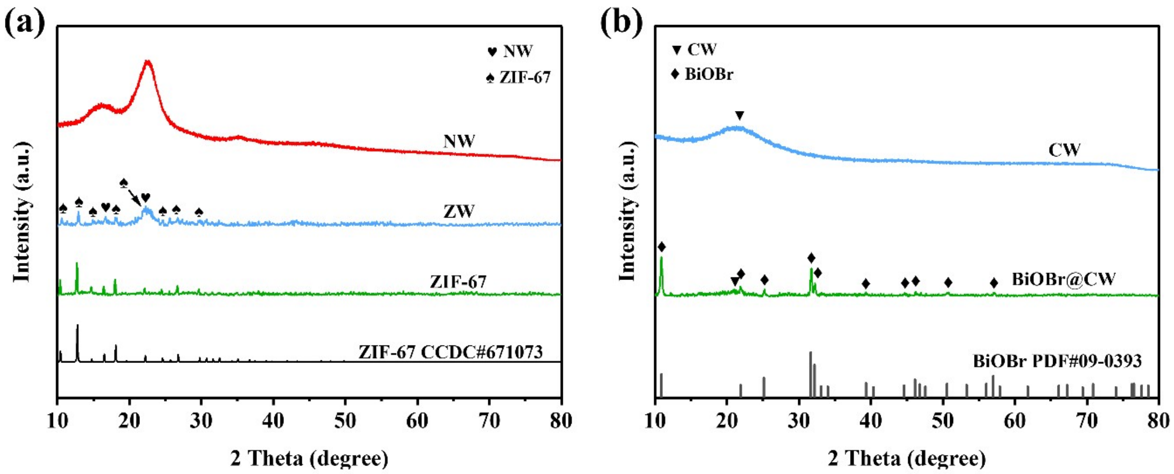

Fig. S5 XRD spectra of (a) NW, ZW, ZIF-67, (b) CW, and BiOBr@ZCW.

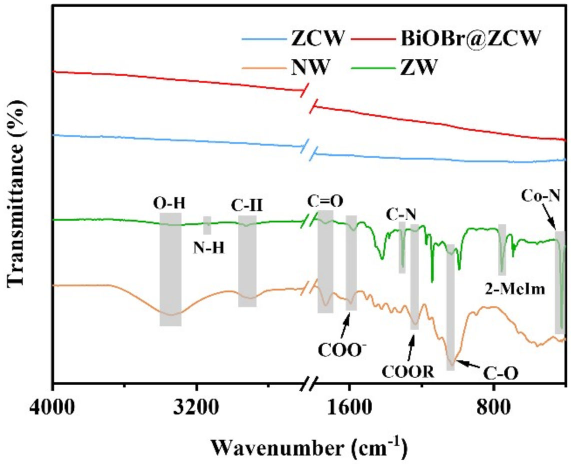

Fig.S6 FTIR spectra of NW, ZW, ZCW, and BiOBr@ZCW.

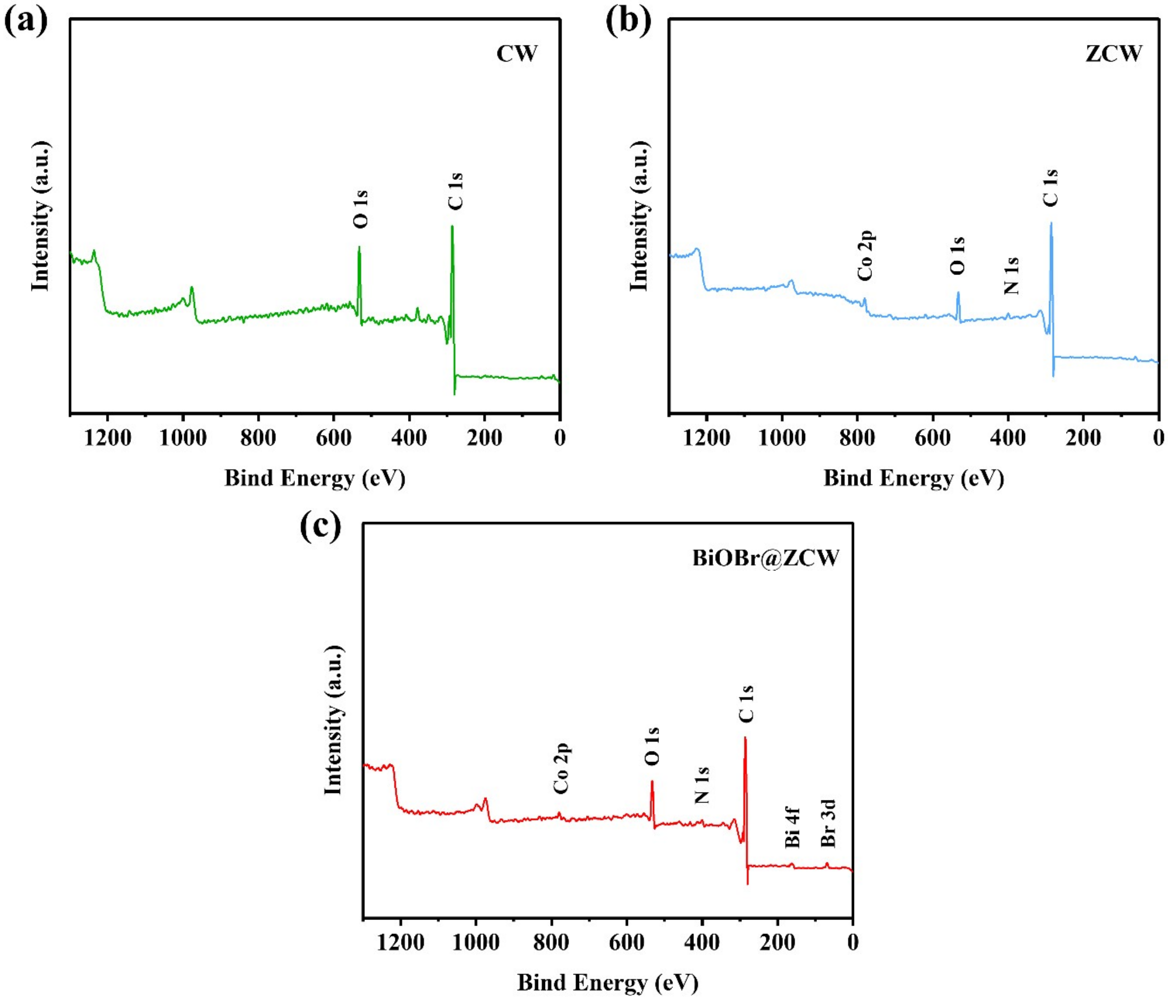

Fig. S7 Survey XPS spectra of (a) CW, (b) ZCW, and (c) BiOBr@ZCW.

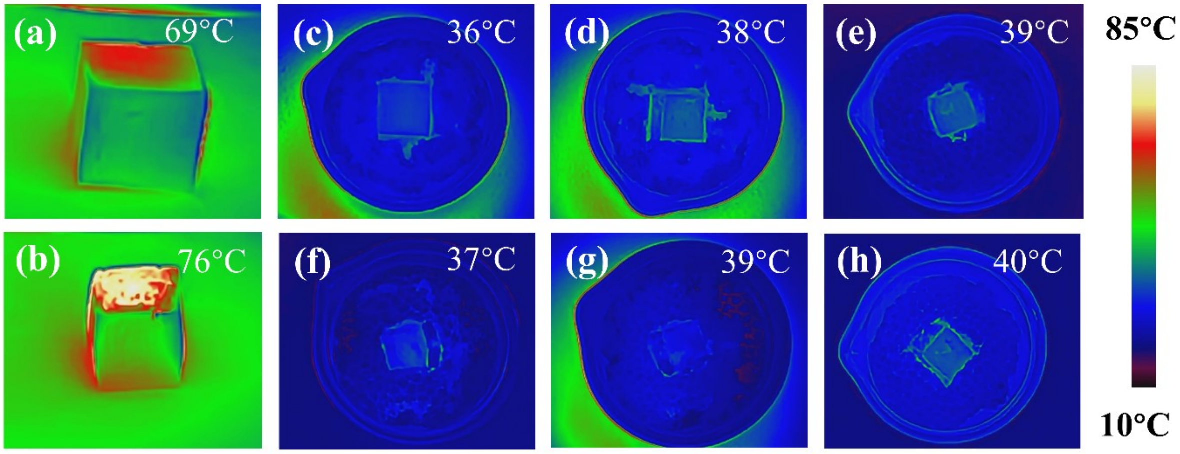

Fig. S8 Infrared photos of (a) NW and (b) CW in dry over time under 1 sun illumination; Infrared photos of (c) NW, (d) CW, (e) ZCW, (f) BiOBr, (g) BiOBr@CW, and (h) BiOBr@ZCW in water over time under 1 sun illumination.

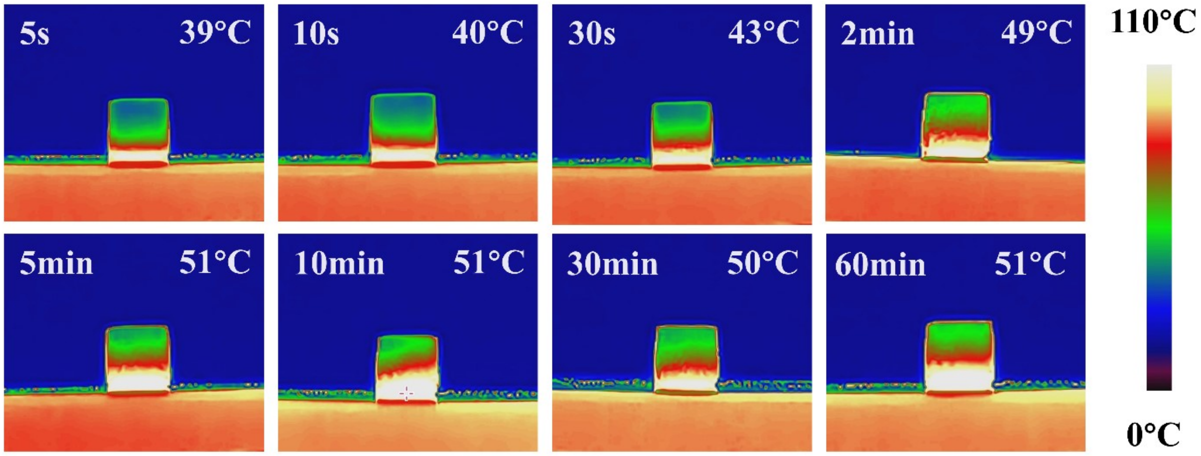

Fig. S9 Infrared photos of BiOBr@ZCW cross section placed in a magnetic stirrer and heated to 90°C in 1 hour.

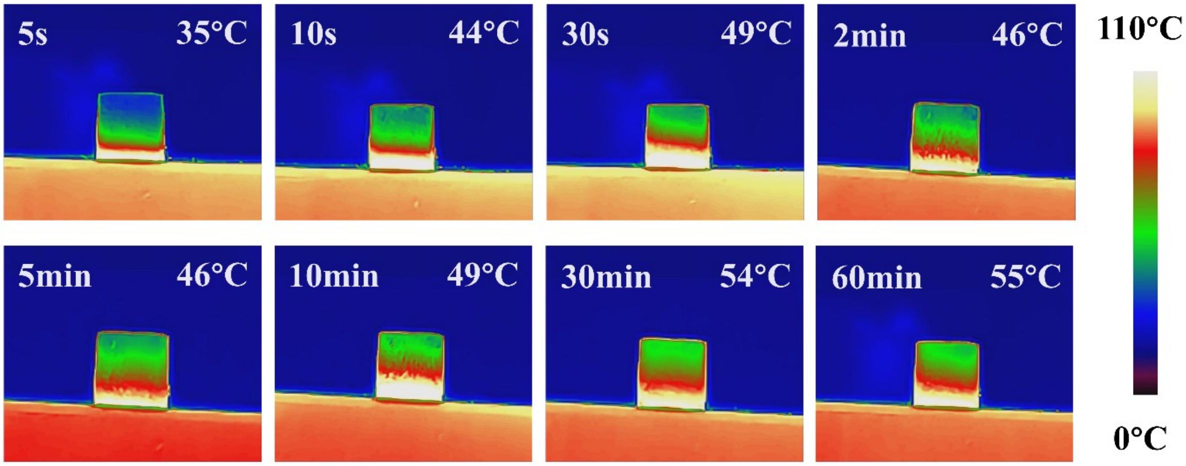

Fig. S10 Infrared photos of BiOBr@ZCW tangential section placed in a magnetic stirrer and heated to 90°C in 1 hour.

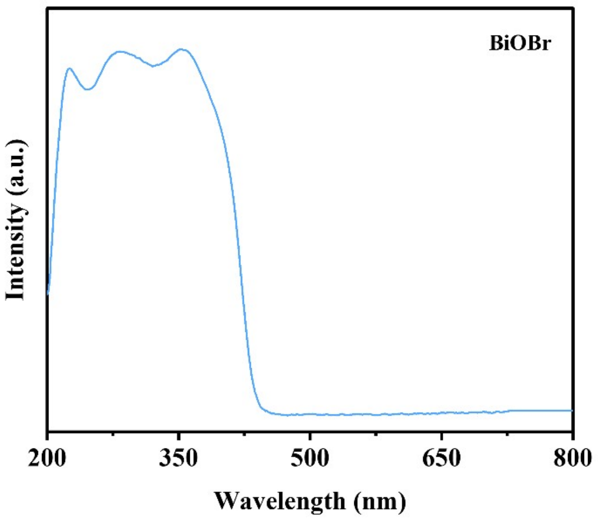

Fig. S11 UV-vis DRS spectra of BiOBr.

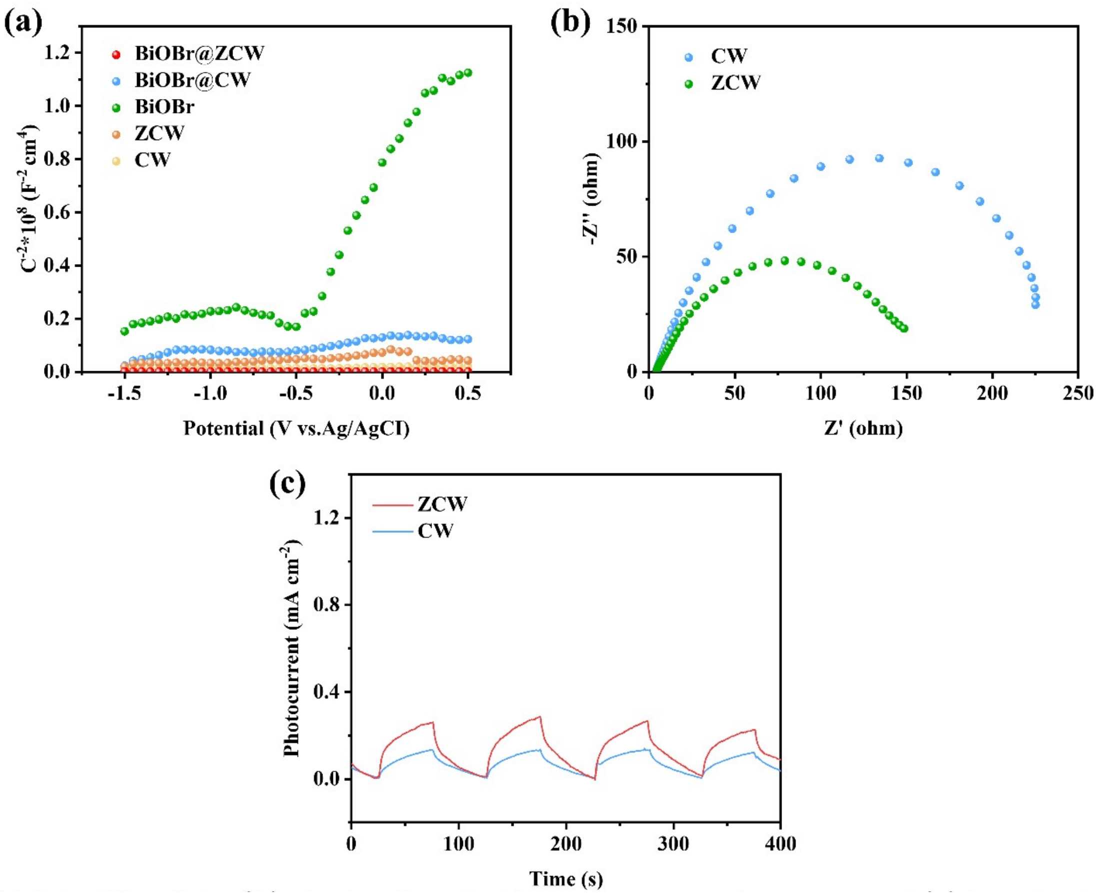

Fig. S12 (a) Mott-Schottky plots, (b) electrochemical impedance spectroscopy and (c) transient photocurrent responses of different samples.

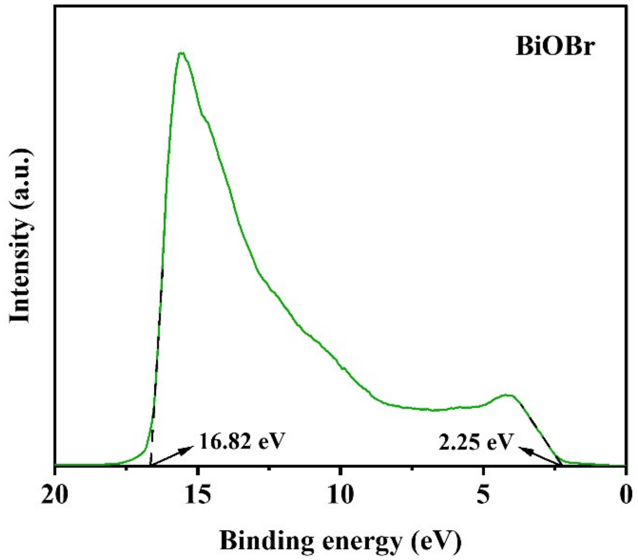

Fig. S13 Ultraviolet photoelectron (UPS) spectra of BiOBr.

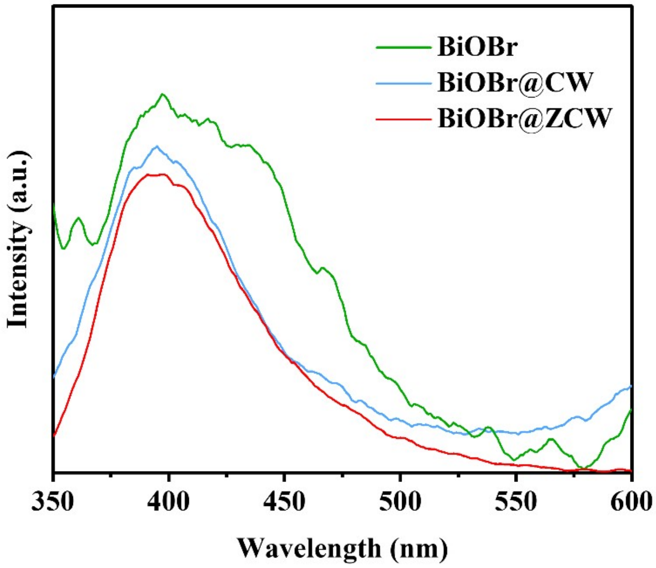

Fig. S14 Normalized photoluminescence (PL) spectra of BiOBr, BiOBr@CW, and BiOBr@ZCW.

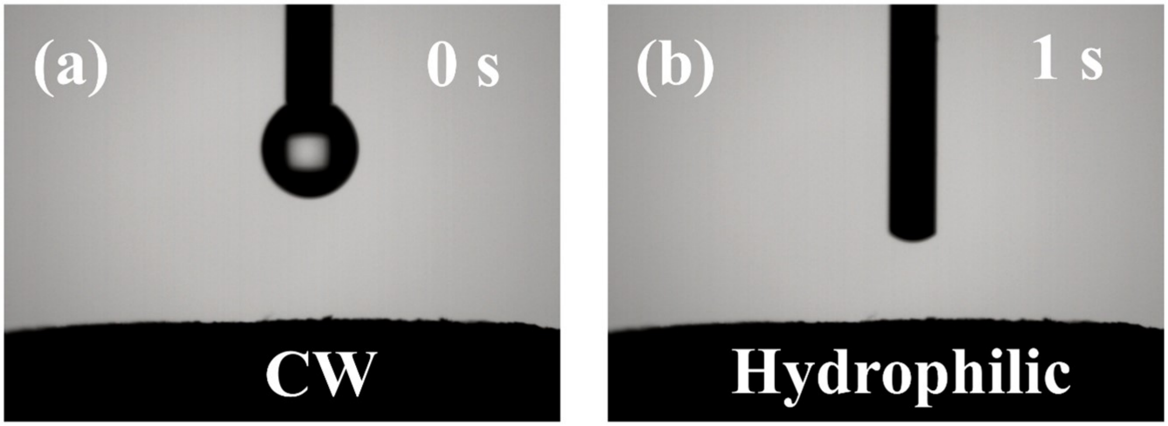

Fig. S15 Water contact angles on CW.

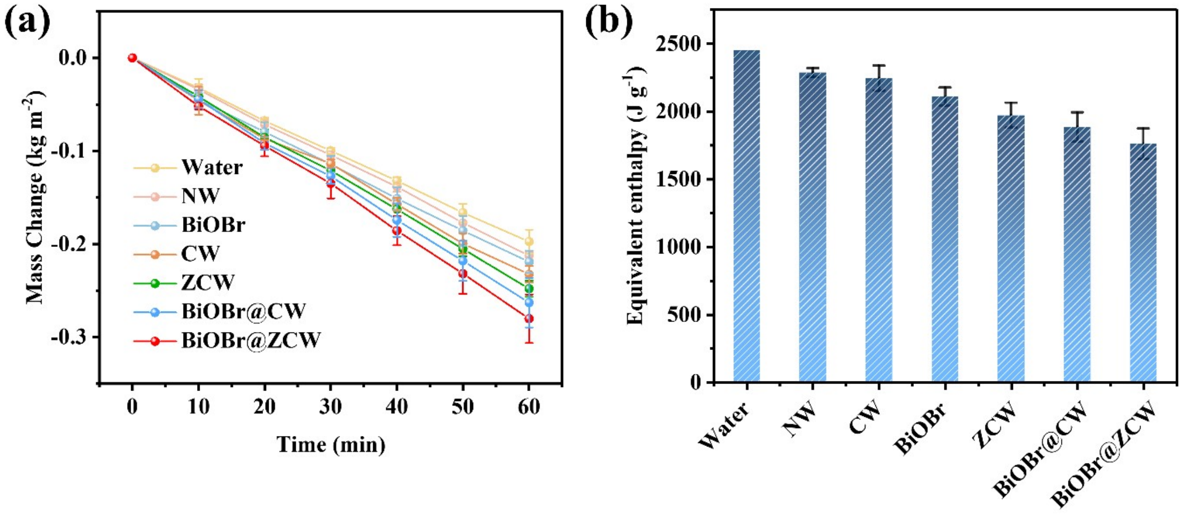

Fig. S16 (a) Mass loss in water over time in the dark. (b) Equivalent enthalpy of water, NW, CW, BiOBr, ZCW, BiOBr@CW, and BiOBr@ZCW.

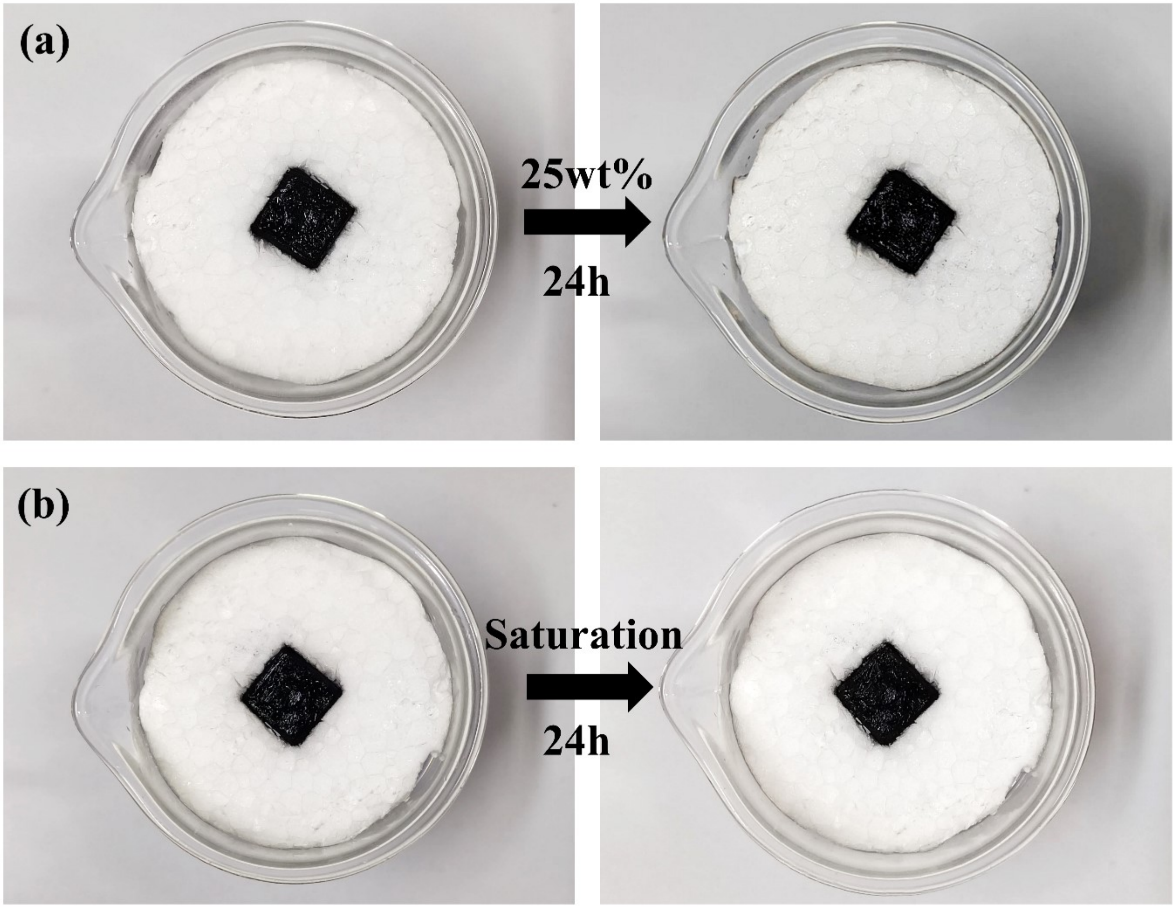

Fig. S17 Digital photograph of evaporator surface without salt crystals evaporating in (a) 25 wt% and (b) saturation brine for 24 h.

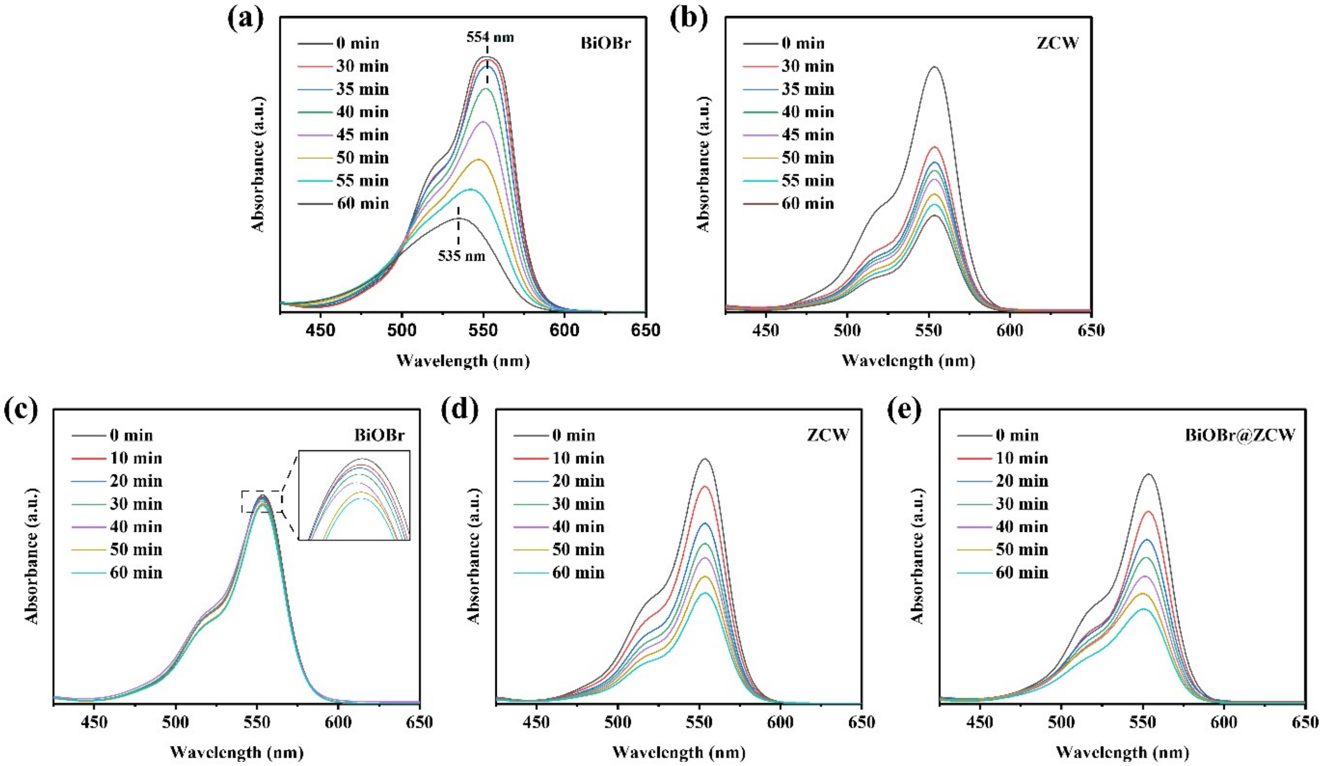

Fig. S18 UV-vis absorption spectra of RhB solution recorded under 1 sun light for samples of (a) BiOBr and (b) ZCW; UV-vis absorption spectra of RhB solution with (c) BiOBr, (d) ZCW, and (e) BiOBr@ZCW under dark environments.

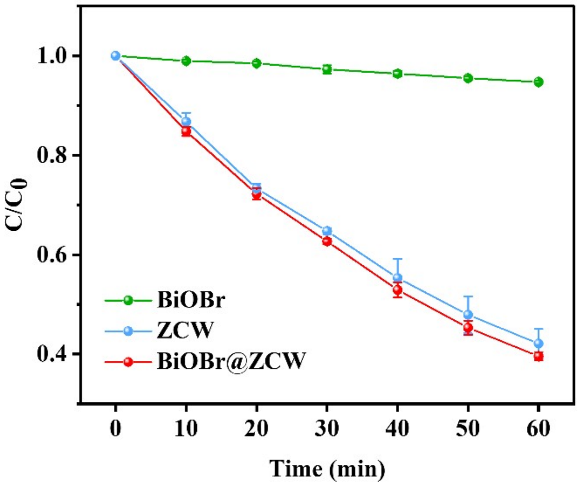

Fig. S19 Dark adsorption-degradation curves of BiOBr, ZCW, and BiOBr@ZCW.

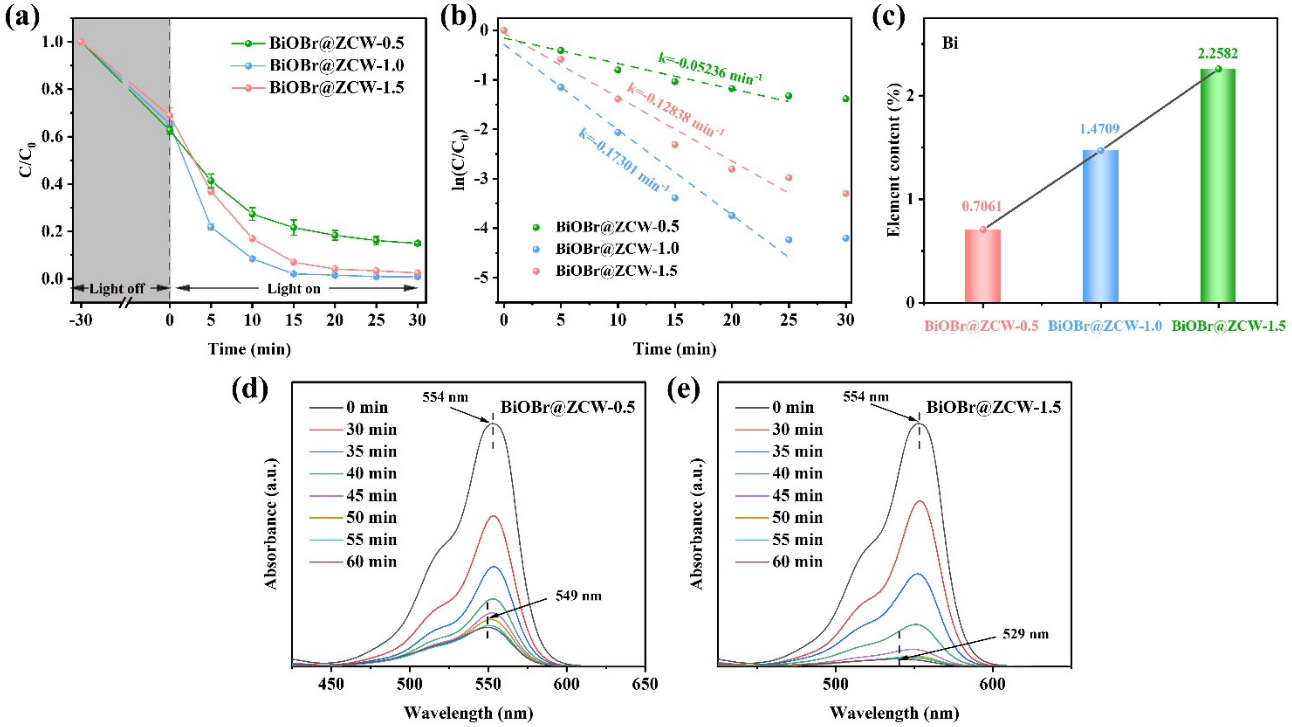

Fig. S20 (a) Photocatalytic degradation curves, (b) primary kinetic curves and (c) corresponding bismuth content curve of samples with different BiOBr loadings; UV-vis absorption spectra of RhB solution recorded under one sun light for samples of (d) BiOBr@ZCW-0.5 and (e) BiOBr@ZCW-1.5.

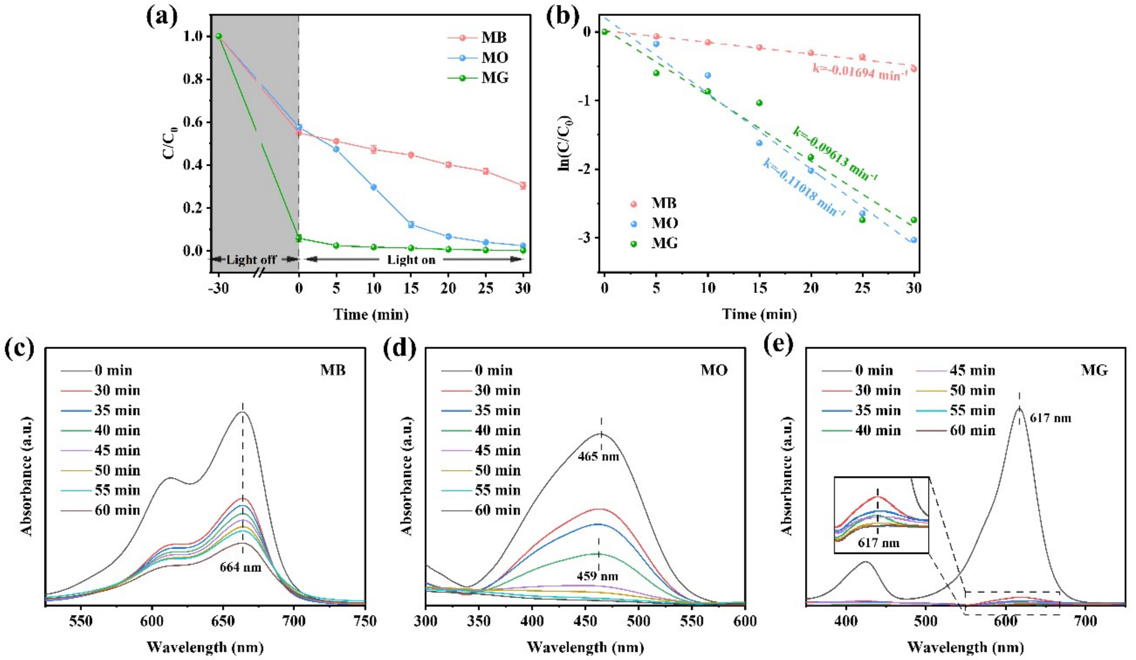

Fig. S21 (a) Photocatalytic degradation curves and (b) primary kinetic curves of different dyes; UV-vis absorption spectra of (c) MB, (d) MO and (e) MG with BiOBr@ZCW recorded under one sun light.

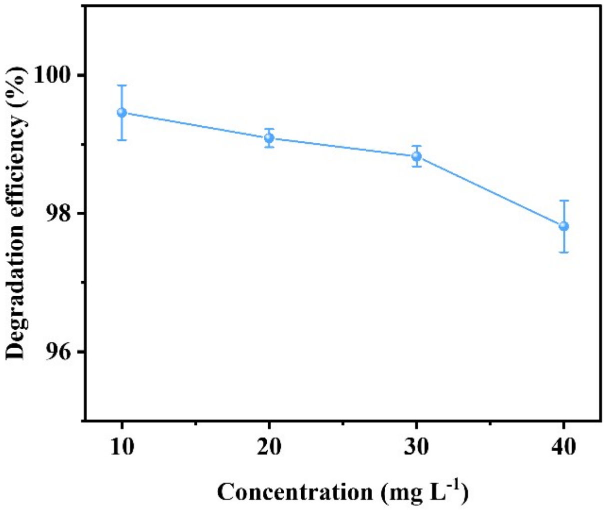

Fig. S22 Degradation efficiency curves of BiOBr@ZCW under the different concentration of RhB.

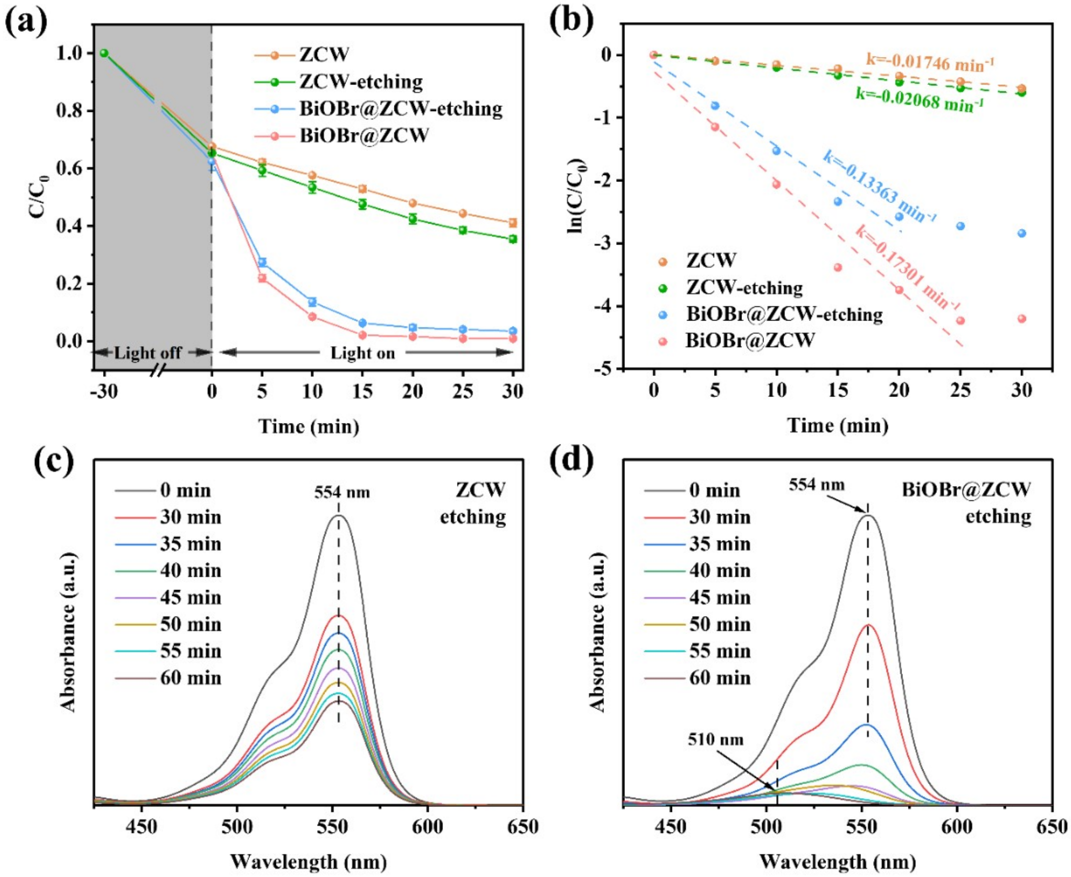

Fig. S23 (a) Photocatalytic degradation curves and (b) primary kinetic curves of different samples etching with HCl; UV-vis absorption spectra of visible light driven photodegradation RhB via use of (c) ZCW and (d) BiOBr@ZCW after etching.

To further evaluate the contribution of metallic Co in enhancing photodegradation performance, we prepared BiOBr@ZCW-etching and ZCW-etching samples by etching BiOBr@ZCW and ZCW with HCl. The photodegradation performance of these samples was subsequently tested against RhB. As shown in Fig. S23a and b, the ZCW-etching sample exhibited enhanced RhB removal performance, whereas the BiOBr@ZCW-etching sample demonstrated reduced RhB removal efficiency. This difference arises because HCl etching removed metallic Co from ZCW, resulting in a larger specific surface area for ZCW-etching, which is beneficial for the adsorption and removal of RhB from the solution. In contrast, the reduction of metallic Co in BiOBr@ZCW-etching hinders the separation of photogenerated charges in BiOBr, leading to a decrease in the generation of highly reactive $\cdot O_2^-$ species and, consequently, a reduction in RhB photodegradation activity.

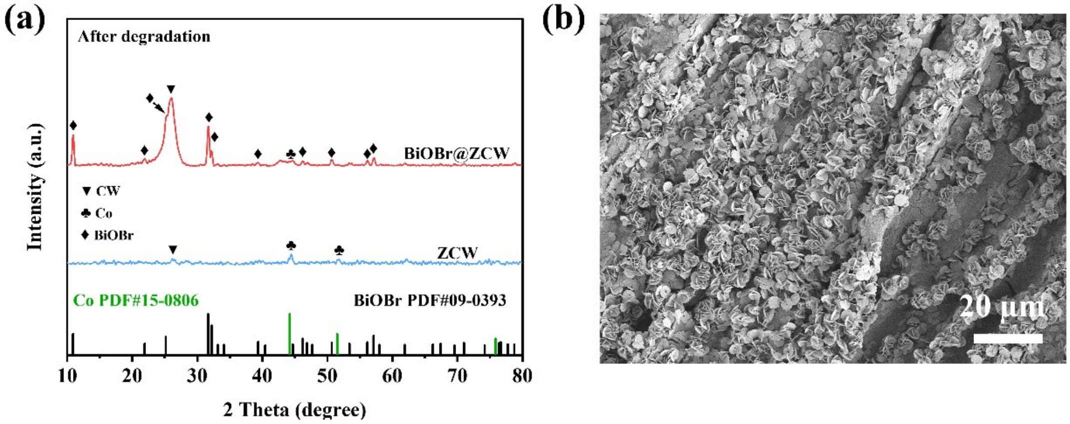

Fig. S24 (a) XRD patterns of ZCW and BiOBr@ZCW and (b) SEM of BiOBr@ZCW in the treated water after cyclic experiments.

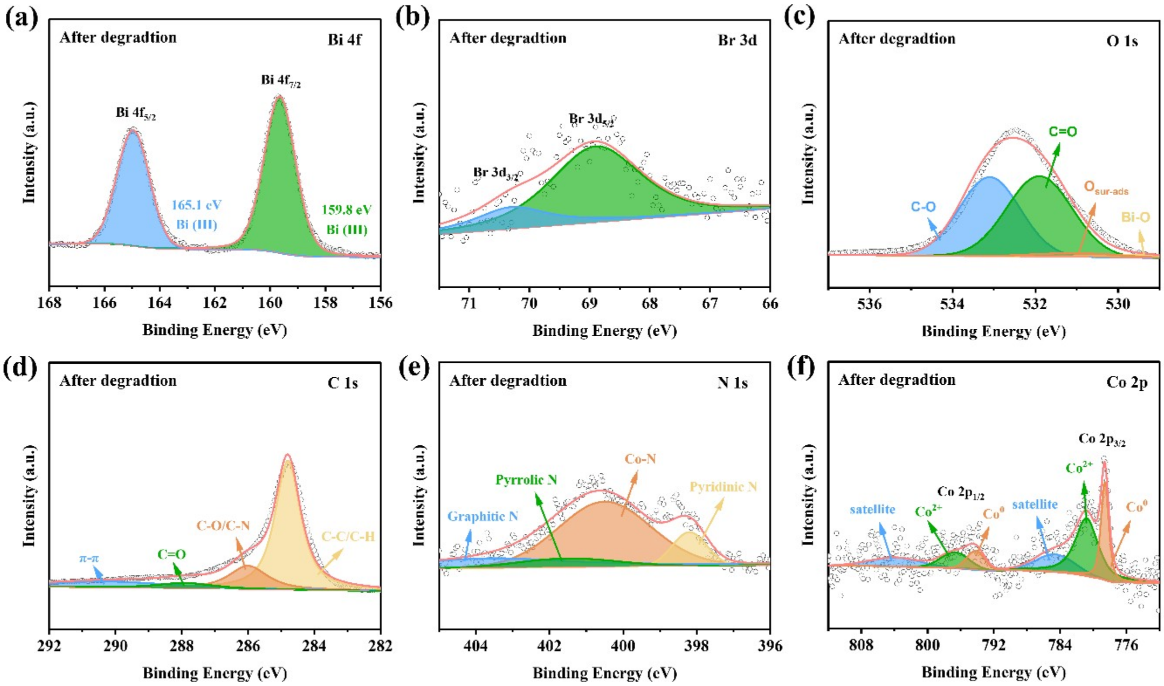

Fig. S25 High-resolution XPS spectra of (a) Bi 4f, (b) Br 3d, (c) O 1s, (d) C 1s, (e) N 1s, and (f) Co 2p of BiOBr@ZCW in the treated water after cyclic experiments.

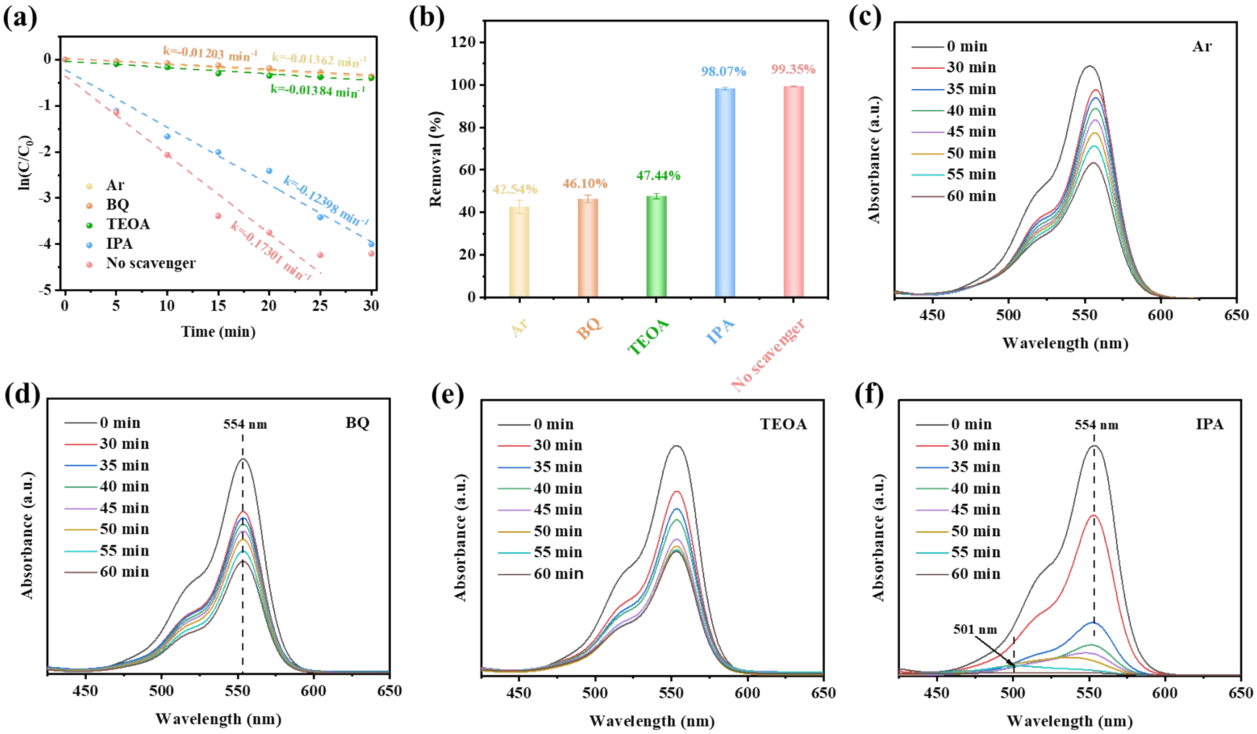

Fig. S26 (a) primary kinetic curves and (b) corresponding removal rates of RhB by adding different sacrificial agents for BiOBr@ZCW; UV-vis absorption spectra of visible light driven photodegradation RhB by adding (c) Ar, (d) BQ, (a) TEOA and (b) IPA via use of BiOBr@ZCW.

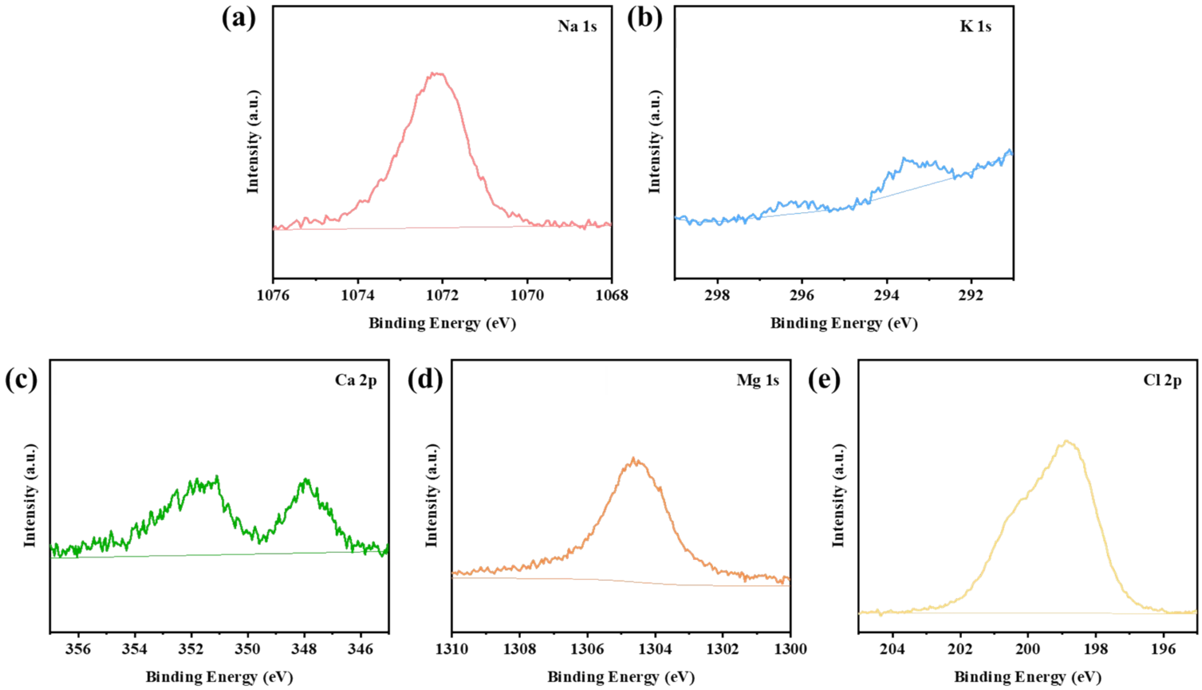

Fig. S27 High-resolution XPS spectra of (a) Na 1s, (b) K 1s, (c) Ca 2p, (d) Mg 1s and (f) Cl 2p of BiOBr@ZCW after the outdoor evaporation experiment.

Table S1 Comparison of solar steam generation capability of BiOBr@ZCW evaporator and the reported evaporators based on wood materials under 1 sun.

Materials	**Evaporation rates (kg m^{-2} h^{-1})**	**Reference**
wood-based capillary enhancer	1.217	*J. Colloid Interface Sci.*, 2024, **653**, 454-462
MnO_2/wood	1.22	ACS Appl. Energ. Mater., 2021, **4**, 1752-1762
Fe_3O_4/PVA delignified wood	1.30	*Desalination*, 2021, **507**, 115024
Janus wood	1.35	*Energy Environ. Sci.*, 2021, **14**, 5347-5357
wood supported 3D-hierarchical Cu_3SnS_4	1.35	*J. Colloid Interface Sci.*, 2022, **615**, 707-715
wood aerogel after surface carbonization	1.40	*Sol. Energy*, 2021, **227**, 303-311
CNT@wood sponges	1.45	*ACS Appl. Mater. Interfaces*, 2023, **15**, 38100-38109
Ag-Cu/sawdust-derived biochar@PVA	1.49	*Desalination*, 2022, **535**, 115824
TiO_2/CN-decorated wood carbon	1.49	*J. Clean Prod.*, 2022, **365**, 132827
rGO/carbonized wood	1.492	Sustain. Energy Technol. Assess., 2023, **57**, 103199
Ag/$MgFe_2O_4$@surface carbonized wood	1.55	Small, **2024**, e2309087
BiOBr@ZCW	**1.67**	**This work**